Journal of Materials Chemistry A

Understanding Cation-Disordered Rocksalt Oxyfluoride Cathodes

Journal:	*Journal of Materials Chemistry A*
Manuscript ID	TA-ART-12-2020-012179.R1
Article Type:	Paper
Date Submitted by the Author:	24-Feb-2021
Complete List of Authors:	Chen, Dongchang; Lawrence Berkeley National Laboratory Ahn, Juhyeon; Lawrence Berkeley National Laboratory, ESDR Self, Ethan; Oak Ridge National Laboratory, Nanda, Jagjit; oak ridge national laboratory, Materials Science & Technology Divison Chen, Guoying; Lawrence Berkeley National Laboratory, ESDR

SCHOLARONE™
Manuscripts

Understanding Cation-Disordered Rocksalt Oxyfluoride Cathodes

Dongchang Chen,[a] Juhyeon Ahn,[a] Ethan Self,[b] Jagjit Nanda[b] and Guoying Chen[a,]*

[a.] *Energy Storage and Distributed Resources Division, Lawrence Berkeley National Laboratory, Berkeley, California 94720, USA*

[b.] *Chemical Science Division, Oak Ridge National laboratory, Oak Ridge, TN 37831 USA*

** Corresponding author's email: gchen@lbl.gov*

Abstract

Partial fluorine (F) substitution into the oxygen (O) sublattice has been shown to improve cycling stability of cation-disordered Li-excess rocksalt oxide (DRX) cathodes. Detailed understanding on failure mechanisms and key optimization knowledge of fluorinated-DRX (F-DRX), however, are lacking. In the present study, we incorporate different amounts of F into a baseline DRX system, $Li_{1.2}Ti_{0.4}Mn_{0.4}O_2$ (LTMO3.0, 3.0 denotes nominal Li/Mn ratio), and synthesize two oxyfluoride compounds, Li-rich $Li_{1.3}Ti_{0.3}Mn_{0.4}O_{1.7}F_{0.3}$ (LTMOF3.25) and Mn-rich $Li_{1.2}Ti_{0.2}Mn_{0.6}O_{1.8}F_{0.2}$ (LTMOF2.0) with an increased and reduced Li/Mn ratio of 3.25 and 2.0, respectively. Through careful monitoring of chemical and structural evolution, we show that cycling-induced changes are manifested not only by Mn reduction and degradation of its local coordination environment, but also by F enrichment and formation of LiF-type of domains on the surface. A "concerted-densification" based failure mechanism, involving atomic-level changes in both transition-metal cationic sublattice and oxygen/fluorine anionic sublattice, is proposed for the degradation in F-DRX cathode materials. The study reveals that increasing F content accompanied

by reduced Li/Mn ratio mitigates the degradation process, offering key design strategies in achieving balanced cathode capacity and stability.

1. Introduction

Development of advanced cathode materials with higher energy density, improved safety, and lower cost largely determines the future of the Li-ion battery (LIB) industry.[1-4] The classic layered oxide cathodes such as lithium nickel manganese cobalt oxides ($LiNi_xMn_yCo_{1-x-y}O_2$, NMCs) have limited energy density. Their need for cobalt also brings about controversial ethical issues in the mining and sourcing industry. In recent years, Li-rich cation-disordered rocksalts (denoted as DRX) have attracted great attention as a promising new class of Co-free LIB cathodes.[5-8] Research so far has revealed a wide chemistry space for DRX compounds capable of delivering high specific energy >1000 Wh/kg.[6,8] In general, the high capacities arise from the combination of both transition-metal (TM) cationic and oxygen anionic redox activities.[7,9-12] Extensive involvement of oxygen redox, however, leads to challenging performance issues, including capacity fade, impedance rise, and voltage fade after cycling.[13-21]

Recently, F substitution into the oxygen sublattice was demonstrated as a new approach to mitigate the performance issues.[6,22-27] Such a strategy was implemented in various DRX cathodes with a range of compositions, including the fluorination of Nb-Mn [24,28] and Ti-Mo-Ni [22] based systems. The rocksalt structure of DRX oxides is made up of a metal cationic sublattice and an oxygen anionic sublattice. The cationic sublattice typically consists of a redox-active TM (e.g., Mn, Ni, V, etc.), a redox-inactive d^0 TM (e.g. Nb, Ti, Ta etc.) and Li cations. All cations occupy the octahedral sites in a random fashion within the sublattice. [9,29] The replacement of O^{2-} with F^- decreases the total charge in the anionic sublattice which creates the freedom to tune the stoichiometry of the cationic sublattice components. As the redox-inactive TM is inert and therefore should be kept in minimum, charge compensation can be achieved by either increasing the Li content or redox-active TM content. Despite the impressive theory work and synthesis

progress made in the oxyfluoride compounds, fluorinated DRX (F-DRX) cathodes reported so far continue to suffer from performance decay. The lack of understanding in failure mechanism and the key knowledge needed for materials optimization have hindered development of F-DRX cathodes.

In our previous work, we investigated a DRX oxide, $Li_{1.3}Nb_{0.3}Mn_{0.4}O_2$, and revealed the effect of redox-inactive TM on cathode degradation.[11,30] Here, we prepared two oxyfluoride compounds, Li-rich $Li_{1.3}Ti_{0.3}Mn_{0.4}O_{1.7}F_{0.3}$ (LTMOF3.25) and Mn-rich $Li_{1.2}Ti_{0.2}Mn_{0.6}O_{1.8}F_{0.2}$ (LTMOF2.0), based on the Li-Ti-Mn-O (LTMO) system. The baseline compound, $Li_{1.2}Ti_{0.4}Mn_{0.4}O_2$ (LTMO3.0), can be expected to behave similarly to $Li_{1.3}Nb_{0.3}Mn_{0.4}O_2$. The value shown in each sample label corresponds to Li/Mn molar ratio in the formula. Compared to the baseline material LTMO3.0, LTMOF3.25 and LTMOF2.0 correspond to an increased and decreased Li/Mn ratio of 3.25 and 2.0, respectively. We compare the electrochemical performance of these cathodes and evaluate structural changes which occur during cycling. Our results demonstrate that electrochemical cycling causes material densification involving atomic rearrangement in both cationic and anionic sublattices in F-DRX. Strategies to mitigate these changes are also demonstrated.

2. Results and discussion

2.1 Synthesis, properties and electrochemical performance

The LTMO3.0 baseline sample was synthesized by using a molten-salt method described in detail in our previous publications.[11,14] Phase-pure discrete rocksalt particles with an average particle size of ~ 3-5 μm were obtained from the KCl flux, as confirmed by the X-ray diffraction

(XRD) pattern and scanning electron microscopy (SEM) image shown in Figure S1a and S1b, respectively. The oxyfluorides were prepared using a solid-state self-flux method where LiF (m.p.= 850 ^{o}C) was used as both F source and a flux for crystal growth. Typically, an excess of LiF (150 - 200 mol.%) and Li_2CO_3 (110-115 mol.%) were used to compensate for Li loss during calcination at high temperature.

Upon the incorporation of F^- into the O^{2-} sublattice in LTMO3.0, charge compensation can be achieved by either increasing Mn content (Mn-rich) and lowing Li/Mn ratio or increasing both Li content (Li-rich) and Li/Mn ratio. Here, two samples with different levels of LTMO fluorination, Li-rich $Li_{1.3}Ti_{0.3}Mn_{0.4}O_{1.7}F_{0.3}$ (LTMOF3.25) and Mn-rich $Li_{1.2}Ti_{0.2}Mn_{0.6}O_{1.8}F_{0.2}$ (LTMOF2.0), were prepared in a higher and lower Li/Mn ratios of 3.25 and 2.0, respectively. Figure 1 shows the X-ray and neutron diffraction patterns collected on the as-synthesized samples. Both were highly crystalline single-phase rocksalts without the presence of impurities (Figure 1a-d). The lattice parameters obtained from the joint XRD and neutron refinements were 4.1577 Å for LTMOF3.25 and 4.1572 Å for LTMOF2.0, which is comparable to that of LTMO3.0 (4.1571 Å). Figure 1e and 1f show SEM images and elemental mapping results obtained from energy dispersive X-ray (EDX) analysis. Fluorination leads to a growth in the discrete particles, with the average size of both samples at ~ 20 μm as opposed to ~ 5 μm in LTMO3.0. Overall, uniform elemental distribution of Ti, Mn, O and F were observed at the sub-particle level. The appearance of "darker" regions on the O and F EDX maps is a result of shallow penetration depth of emitted X-ray from the lighter elements. The determined elemental ratios were consistent with the targeted compositions, which were further confirmed by the inductively coupled plasma - optical emission spectrometry (ICP-OES) and F ion selective electrode (F-ISE) measurements. Detailed analysis results are summarized in Table S1.

To evaluate electrochemical performance, the as-prepared rocksalts were first ball-milled with a carbon additive in a weight ratio of 8:2 which breaks down the large particles to a similar average particle size of ~ 1 μm for all samples.[11,28,30] In fabricating the composite cathodes, the prepared mixture was then blended with a carbon additive and a PVdF binder in a weight ratio of 7:2:1. The fraction of the active mass loading in the electrode is therefore 56 wt.%. Fig. 2a-c compares the voltage profiles of LTMOF3.25 and LTMOF2.0 along with the baseline LTMO3.0 cathodes when cycled between 1.5-4.8 V at a specific current of 10 mA/g. In the baseline LTMO3.0, the 1st charge voltage curve displays a sloping region at low voltages and a distinct "flatter" region at high voltages. Based on previous studies on Mn-based DRX,[15] these regions are primarily attributed to the cationic Mn redox and anionic O redox, respectively, with the latter involving the oxidation of O^{2-} to O^{n-} ($0 \leq n < 2$) and O_2 gas evolution.[11,28,30] Fluorination leads to an overall smoother voltage profile and reduces the extent of O redox region, especially in LTMOF3.25. The theoretical capacities based on the total Li content per formula unit are 385, 444 and 395 mAh/g for LTMO3.0, LTMOF3.25 and LTMOF2.0, respectively, of which 131, 152 and 192 mAh/g comes from the contribution of Mn^{3+}/Mn^{4+} redox couple.

The discharge capacity, average voltage and energy are shown in Figure 2d-f. Their retention as a function of cycle number, determined based on the ratios relative to the values obtained at the 1st cycle, is also shown in Figure S2. In the baseline LTMO3.0, the obtained 1st cycle discharge capacity was ~ 200 mAh/g which decreased to 140 mAh/g after 50 cycles (Figure 2d), corresponding to a capacity retention of ~ 70% (Figure S2a). As a result of higher Li content, the initial discharge capacity increased to 240 mAh/g in LTMOF3.25. After 50 cycles, ~165 mAh/g remained which corresponds to the same capacity retention of ~ 70%. For LTMOF2.0, the initial capacity is comparable to that of the baseline. However, it increased slightly during the first

30 cycles, after which it decreased at a relatively slow rate. After 50 cycles, a capacity retention of ~ 95% was achieved. Similar trends were observed on average discharge voltage (Figure 2e) and voltage retention (Figure S2b). While the 1st cycle discharge voltages were comparable at ~ 3.1-3.2 V for all three cathodes, the retention was much improved in the F-DRXs, reaching 83% and 87% for LTMOF3.25 and LTMOF2.0, respectively, as compared to 77% in the baseline after 50 cycles. As a result, significant improvement in both discharge energy and energy retention were observed on F-DRXs, as shown in Figure 2f and Figure S2c. The 1st cycle discharge energy densities were 608, 764 and 646 Wh/kg while the 50th cycle energy retention were 52%, 56% and 77% for LTMO3.0, LTMOF3.25 and LTMOF2.0, respectively.

In DRX oxide cathodes, an increase in Li/Mn ratio generally leads to higher capacity and energy due to increased O redox contribution. However, this often comes with a detrimental effect on cycling stability and more severe discharge capacity and energy fade.[11] Here we show that in the presence of fluorine, Li-rich LTMOF3.25 with the same Mn content as LTMO3.0 delivered more initial discharge capacity without compromising capacity retention, demonstrating that fluorine substitution alleviates performance degradation and allows more reversible cycling of DRX cathodes.

Note that capacity increase upon cycling of LTMOF2.0 cathode is an interesting phenomenon also observed on other Mn-rich DRX materials.[19,28] Our initial investigation suggests that with cycling, local domains of spinel can gradually form within the rocksalt phase. Such phase transformation is largely similar to what occurs between orthorhombic LiMnO2 and the spinel phase, which also leads to capacity increase.[31] We are currently performing systematic studies on a series of samples and the results will be reported in a future publication.

2.2 Structural and chemical evolution with cycling

2.2.1 Cationic sublattice - In our previous work, performance degradation in one of the DRX materials, $Li_{1.3}Nb_{0.3}Mn_{0.4}O_2$, was investigated in detail.[11] It was found that while the valence state of the d^0 TM (Nb, +5) remains unchanged, extensive reduction of the redox-active TM (Mn) occurs during cycling. Similarly, soft X-ray absorption spectroscopy (sXAS) and hard X-ray absorption spectroscopy (hXAS) were used here to probe the TM *L*-edge and *K*-edge, respectively. While the former in the total electron yield (TEY) mode probes about 5 nm on the surface, the latter analyzes the bulk material with a probing depth of a few mm. Figure S3 shows the Ti *L*-edge spectra collected on the pristine electrode as well as the electrodes recovered after 1st charge to 4.8 V and first discharge to 1.5 V. The characteristic Ti(IV) features with the distinctive t_{2g} and e_g bands [32,33] are clearly shown in all spectra, with no detectable changes observed in either in the charged or discharged state. The results confirm that Ti remains redox inactive during cycling, similar to what was observed for Nb in $Li_{1.3}Nb_{0.3}Mn_{0.4}O_2$.

The Mn *L*-edge XAS spectra collected in the discharged state after various cycles are shown in Figure 3a-c. It is well known that Mn at a specific oxidation state displays distinctive *L*-edge spectral features.[34,35] As all spectra were collected in the TEY mode, here changes in surface Mn oxidation state can be monitored. While the spectra from the pristine samples show only Mn(III) features, considerable Mn(II) presence was detected on both oxide and oxyfluoride cathodes, even after the first discharge. As the cycle number increased, the spectra features become more similar to that of Mn(II). The fractions of Mn(II) and Mn(III) as a function of cycle number were obtained through principal component analysis (PCA), and the results are shown in Figure 3d-f. It is evident that with cycling, Mn(II) component increases at the expense of Mn(III). In the baseline LTMO3.0, Mn(II) component accounts for 48%, 73% and 100% after the 1st, 5th and 50th cycle, respectively,

suggesting the full reduction of surface Mn to +2 after 50 cycles between 1.5-4.8 V. Similar results were obtained on LTMOF3.25. For LTMOF2.0, on the other hand, the fractions of Mn(II) were reduced to 33%, 51% and 90% after the 1st, 5th and 50th cycle, respectively, indicating superior chemical stability of surface Mn compared to the other two samples in the series.

Changes in bulk Mn oxidation state were evaluated based on the reflection energy of X-ray near-edge absorption structure (XANES) in the Mn *K*-edge XAS.[36] Figure 4 compares the XANES profiles collected on the oxide and oxyfluoride cathodes at the charged and discharged states after 1, 5 and 50 cycles. For both LTMO3.0 (Figure 4a and 4b) and LTMOF3.25 (Figure 4c and 4d), the absorption edge shifted considerably towards lower energy as the cycle number increased, at both charged and discharged states. However, the edge shift in LTMOF2.0 (Figure 4e and 4f) was much less noticeable. Some changes in XANES profile shape were also observed after cycling, reflecting the changes in transition-metal coordination environment that is often evaluated by extended X-ray absorption fine structure (EXAFS) analysis, as discussed in detail in the following section.

Figure 4g and 4h show the estimated Mn oxidation state as a function of cycle number for the charged and discharged states, respectively. After 50 cycles, similar changes in oxidation state were observed on LTMO3.0 and LTMOF3.25, both of which were reduced from +4 to +3.5 at the charged state and +3 to +2.7 at the discharged state. On the other hand, these values were +3.8 and +2.9 in LTMOF2.0, further confirming its improved bulk chemical stability. The combined results from the XAS studies suggest that DRX fluorination accompanied by reduced Li/TM ratio effectively minimizes chemical changes both in the bulk and near the surface.

Although in the long range, DRX materials have the cation-disordered rocksalt crystal structure, well-defined coordination pairs still exist in the short range. Changes in Mn local

bonding structure, therefore can be examined by analyzing the *K*-edge EXAFS. As shown in Figure S4a, the pristine rocksalt structure shows two main peaks that correspond to two coordination pairs: the peak located at 1.4 Å corresponds to Mn-O coordination (i.e. the first coordination shell) and the peak located at 2.7 Å corresponds to Mn-TM coordination (i.e. the second coordination shell).[37] Simulation of EXAFS spectrum using the rocksalt model (Figure S4b) produced excellent fit for the experimental data.

Mn *K*-edge EXAFS profiles collected on LTMO3.0, LTMOF3.25 and LTMOF2.0 cathodes at the charged state and discharged state after various cycles are shown in Figure 5. For both LTMO3.0 (Figure 5a and 5b) and LTMOF3.25 (Figure 5c and 5d), cycling leads to peak shifting and broadening of Mn-O and Mn-TM coordination at charged and discharged states. After extended cycling, the intensities of the coordination peaks also decrease, suggesting an overall degradation in coordination spheres. On the other hand, the EXAFS profiles collected on the LTMOF2.0 electrodes (Figure 5e and 5f) show minimum changes. After 50 cycles, both Mn-O and Mn-TM coordination peaks were well preserved with negligible peak splitting and broadening. The results suggest that DRX fluorination accompanied by reduced Li/TM effectively mitigates cycling-induced degradation in local coordination environment.

2.2.2 Anionic sublattice – To evaluate the anionic sublattice in F-DRX, F *K*-edge XAS was used to probe the chemical and structural changes.[38] The typical spectrum consists of a pre-edge, an absorption edge and a post-edge that correspond to the transitions from F_{1s} to higher electronic states, including TM_{3d}, F_{2p} and F_{4s4p}. Due to its high electronegativity, F often carries a nominal negative charge. However, depending on the specific compounds, F *K*-edge spectra can vary significantly. For example, F in LiF carries a static negative charge and the bonding environment

is ionic. As shown in Figure 6a, the highly localized charge accumulated at F center leads to *K*-edge XAS spectrum with no obvious features in the pre-edge region and a sharp edge centered near 691 eV, along with several broad peaks in the post-edge region (F_{1s} to continuum) between 710-730 eV. In contrast, F *K*-edge XAS spectrum collected on pristine LTMOF2.0 oxyfluoride rocksalt displays one broad peak centered near 692 eV with no additional peaks, consistent with the highly delocalized nature in electron distribution, or high covalency between F and its neighbors (Figure 6b).

Figure 6c compares F *K*-edge XAS profiles collected on pristine and discharged LTMOF2.0 cathodes after various cycles. All spectra were collected in the TEY mode which probes a surface depth of ~ 5 nm. Compared to the pristine sample, the spectrum collected after the 1st cycle shows noticeable changes with sharper peaks as well as the appearance of the broad feature between 710-730 eV. Further cycling exacerbates these changes, with the spectrum collected after 50 cycles clearly showing the characteristics of LiF. Quantification was achieved by PCA analysis where the F *K*-edge spectra were fitted with the spectra of both pristine LTMOF2.0 and LiF (Figure 6a), which represent the covalent and ionic components, respectively. Figure 6d shows the evolution of ionic (LiF component) fraction as a function of cycle number. It is evident that cycling leads to an increase in ionic character of F on the surface, suggesting the formation and growth of LiF-like domains.

As LTMOF2.0 cathodes were recovered from cells cycled in a 1 M $LiPF_6$ in ethylene carbonate (EC)/diethyl carbonate (DEC) electrolyte, it is possible that F containing species resulting from electrolyte decomposition are also present. In addition, all DRX composite cathodes were prepared with a polyvinylidene fluoride (PVdF) binder which can also contribute to the features in F *K*-edge XAS profile. In order to eliminate these signal interferences and monitor F

changes intrinsic to DRX, control experiments were carried out where LTMOF2.0 cathodes were prepared without the binder. The cathodes were then cycled in cells with a 1 M $LiClO_4$ in propylene carbonate (PC)/ dimethyl carbonate (DMC) electrolyte. F *K*-edge XAS spectrum collected on the discharged cathode after 1st cycle is shown in Figure S5. Although the signal-to-noise ratio is much lower compared to the counterpart cycled in the $LiPF_6$ electrolyte, it is evident that LiF-like spectral features are also shown in the sample, confirming that the observed spectral changes are intrinsic to the F in the DRX cathodes.

2.3 F-DRX degradation mechanism and mitigating strategies

We previously investigated performance deterioration in a related DRX oxide cathode material, $Li_{1.3}Nb_{0.3}Mn_{0.4}O_2$, and proposed a densification-based degradation mechanism.[11] Upon electrochemical cycling, the loss of oxygen from the anionic sublattice facilities TM reduction and the subsequent TM migration into the octahedral sites vacated by Li^+. The net effect is surface-initiated TM-enrichment or densification that progresses towards the bulk.[11,13] This process is similar to what was reported on layered oxide cathode materials. In the latter case, the resulting structural disordering/cation mixing and the eventual formation of spinel-like or rocksalt-type phases are readily verifiable through techniques such as TEM, XRD and neutron diffraction. In DRX, as the cations are already disordered to begin with, the migration of transition-metal cations into the Li sites does not lead to phase transformation. In this case, XAS if often used to probe the densification process by revealing the associated changes in electronic states.

The observation of Mn reduction and changes in local structure by soft XAS, XANES and EXAFS studies suggest that similar cationic densification also occurs in the F-DRX cathodes. In addition, the increase in surface F ionic characteristics suggests an accompanying anionic

densification process where F-enrichment or densification also occur. Based on these results, a "concerted-densification" degradation mechanism involving both cationic and anionic sublattices is proposed for the F-DRX cathodes (Figure 7). After the 1st charge, loss of lattice O leads to oxygen vacancies on the surface. This creates a destabilized rocksalt lattice where the uncoordinated Mn^{4+} (γ=0.67 Å) may be reduced to Mn^{3+} (γ=0.785 Å) with a larger ionic radius. The reduced cations may migrate into the neighboring octahedral vacancy sites left by Li^{+} (γ=0.9 Å). The net effect is a densified surface layer with fewer Li vacancies and lower Mn oxidation state compared to that in the bulk. During the subsequent discharge process, Li cations are reinserted into the oxide but the surface has lower Li content due to the densification and loss of Li sites. This process continues in the following cycles and progresses from the surface to the bulk. After extensive cycling, the changes can be seen well into the bulk of the material, as demonstrated by the lower than +3 of Mn oxidation state after 50 cycles (Figure 4). In the meantime, the loss of surface lattice O during charging leads to O deficiency in the anionic sublattice and consequently, F enrichment on the surface. Li^{+} reinsertion upon discharge creates domains resembling LiF. After extended cycling, further enrichment of F and accumulation of LiF-like domains lead to strong ionic-F characteristics in the surface region, as shown by the F *K*-edge XAS results in Figure 6. The concerted cationic and anionic densification process likely creates a resistive surface layer that is detrimental to Li transport and causes performance decay.

Figure 8 summarizes the retention in discharge capacity, discharge energy, and Mn valence after 50 cycles. Compared to the baseline LTMO3.0, fluorination in LTMOF3.25 was compensated by an increase in Li content. Higher initial discharge capacity (Figure 8a) and energy (Figure 8b) were achieved through enhanced capacity contribution from oxygen redox. The improvement, however, did not lead to reduced stability, as the retention in both capacity and

energy appear similar to the baseline. The comparison on the retention of Mn oxidation state during the first 50 cycles (Figure 8c) shows similar trend in both materials, further confirming that fluorination provides beneficial effect on DRX chemical and cycling stabilities.

Further performance improvement was achieved by fluorination compensated by an increase in Mn content, or a lower Li/Mn ratio. As shown in Figure 8, both capacity and energy retention were much improved in LTMOF2.0, and the cathode experienced minimal bulk Mn reduction (from +3 to +2.9) after 50 cycles. As the densification-based degradation process initiates at the surface before progressing towards the bulk, surface Mn reduction remains significant in LTMOF2.0 (Figure 8c). The results suggest that reducing Li/Mn ratio in F-DRX is an effective strategy in mitigating the degradation process.

3. Conclusions

The degradation mechanism of cation-disordered rocksalt oxyfluoride cathode materials was investigated in this study. Model Li-rich LTMOF3.25 and Mn-rich LTMOF2.0 samples were synthesized and compared to the baseline LTMO3.0 oxide cathode. Diagnostic *ex-situ* studies using synchrotron X-ray based techniques revealed that electrochemical cycling leads to reduction of Mn both in the bulk and on the surface, along with the degradation in Mn coordination environment. Fluorination substitution significantly reduces these changes. Cycling also led to fluorine enrichment and the formation of LiF-like domains near the surface. A "concerted-densification" based degradation mechanism, involving changes in both TM (Li/Mn/Nb) cationic sublattice and O/F anionic sublattice, was proposed for F-DRX cathode materials. We further show

that fluorination accompanied by a lower Li/Mn ratio is an effective strategy in improving chemical and cycling stability of F-DRX cathodes.

4. Experimental

4.1 Synthesis

LTMO3.0 oxide was synthesized using a solid-state approach as previously described.[30] LTMOF3.25 and LTMOF2.0 oxyfluorides were synthesized using a solid-state self-flux method. Stoichiometric amounts of Li_2CO_3, TiO_2, Mn_2O_3 (Sigma Aldrich) and LiF (Alfa Aesar) were mixed together with ethanol in a planetary ball mill (RETSCH PM100) at 200 rpm for 18 h. Typically, 110-115 mol.% Li_2CO_3 was used to compensate Li loss during calcination at high temperatures. Excess LiF (150-200 mol.%, m. p. =850 C^o) was added to serve as both F source and the flux for oxyfluoride nucleation and growth. The precursor was dried before heating in an Ar-atmosphere quartz tube furnace at a ramping rate of 4 ^{o}C/min and calcinating at 950 ^{o}C for 12 h. The resulting powder was thoroughly washed with deionized water to remove the residue salts, particularly LiF which has a solubility in water of 127 mg/100 ml. All samples were dried overnight at 80 ^{o}C in a vacuum oven.

4.2 Characterization

Phase purity of obtained powders was analyzed by a Bruker D2 powder X-ray diffractometer (Cu Kα, 40 kV, 30 mA). Rietveld refinements of XRD patterns were performed using the FullProf software. Time-of-flight (TOF) neutron powder diffraction experiments were performed using the POWGEN instrument at the Spallation Neutron Source (Oak Ridge National

Laboratory). The data were collected at 300 K using the frame with a center wavelength of 0.8 Å and bandwidth of 1 Å. Rietveld refinement of the neutron diffraction data was performed using GSASII software package.[42]

Sample morphology was examined by using a scanning electron microscope (JEOL JSM-7500F). ICP measurement was performed using an ICP-OES analyzer (Perkin Elmer OPTIMA 5300). Fluorine contents were determined by using fluorine ion selective electrode (UX-27504-14) measurements. Sodium acetate (Sigma Aldrich) and total ionic strength adjustment buffer solutions (TISAB, Cole Parmer) were used to adjust the pH of the analyte.

Mn *K*-edges *h*XAS measurements were performed at SSRL beamline 2-2 and beamline 4-3. Recovered cycled electrodes were thoroughly rinsed by dimethyl carbonate and dried in a glovebox prior to sample loading. Samples were sandwiched between Kapton films for the measurements. A Si (220) crystal was applied as a monochromator. For XAS acquisition at beamline 2-2, higher harmonics were eliminated by detuning the monochromator by 50% at the Mn *K*-edge. Monochromatic energy calibration was accomplished by the E_0 value of 6539 eV of Mn metal foil reference. XANES data were processed by using the Sam's Interface for XAS Package (SIXPACK) software. EXAFS processing was performed by using the Athena software and EXAFS simulation was performed by using the Artemis software. Soft XAS measurements were carried out at BL 10-1 at SSRL. Samples are loaded onto conductive carbon tapes inside an Ar-filled glovebox which were then attached to an aluminum rod sample holder. Spectral measurements were performed on the 31-pole wiggler with a ring current of 350 mA, a 1000 line mm^{-1} grating monochromator with 20 mm entrance and exit slits, and a 1 mm^2 beam spot. XAS profiles were collected under ultrahigh vacuum (10^{-9} Torr) using the total electron yield detector.

4.3 Electrochemical measurements

For composite electrode preparation, active materials were first ball-milled with acetylene carbon black (Denka) in a weight ratio of 8:2. The ball-milled powder was then added into an NMP solvent together with acetylene carbon black and a PVdF binder (Kynar 2801) in a weight ratio of 7:2:1 and thoroughly mixed. The obtained slurry was casted onto an aluminum foil and dried overnight at 100 °C under vacuum. Cathode disks with an area of 1.6 cm^2 and a typical mass loading of 2-3 mg/cm^2 were used for cell testing in 2032-type coin cells. Half-cells were assembled in an argon-filled glovebox with Li foils (Alfa-Aesar) as counter and reference electrodes and Celgard 2400 membrane as separators. A solution of 1 M $LiPF_6$ in 1:1 (v/v) EC: DEC (Novolyte Technologies Inc.) or 1 M $LiClO_4$ in 1:1 (v/v) PC: DMC were used as the electrolyte. The cells were galvanostatically cycled using a VMP3 multichannel potentiostat/galvanostat. All electrochemical measurements were carried out at room temperature.

Acknowledgements

We thank Drs. Matthew Latimer and Erik Nelson at SSRL for assisting the hard XAS measurements, and Dr. Sam Webb at SSRL for helping with micro-XAS measurements and data analysis. Efforts on soft XAS data acquisition by Dr. Dennis Nordlund is greatly appreciated. Use of the Stanford Synchrotron Radiation Lightsource, SLAC National Accelerator Laboratory is supported by the Office of Science, Office of Basic Energy Sciences of the U.S. Department of Energy under Contract No. DE-AC02-76SF00515. We thank Drs. Jue Liu and Yiman Zhang for helping with neutron diffraction measurements and analysis. Neutron diffraction measurements were conducted at the POWGEN beamline at the Spallation Neutron Source, Oak Ridge National Laboratory, which was sponsored by the Scientific User Facilities Division, Office of Basic

Sciences, U.S. Department of Energy. This work was supported by the Assistant Secretary for Energy Efficiency and Renewable Energy, Office of Vehicle Technologies of the U.S. Department of Energy under Contract No. DE-AC02-05CH11231.

References

1 Whittingham, M. S. Lithium Batteries and Cathode Materials. *Chem. Rev. (Washington, DC, U. S.)* **104**, 4271-4302 (2004).

2 Ellis, B. L., Lee, K. T. & Nazar, L. F. Positive Electrode Materials for Li-Ion and Li-Batteries†. *Chem. Mater.* **22**, 691-714 (2010).

3 Goodenough, J. B. & Kim, Y. Challenges for Rechargeable Li Batteries. *Chem. Mater.* **22**, 587-603 (2010).

4 Manthiram, A., Knight, J. C., Myung, S.-T., Oh, S.-M. & Sun, Y.-K. Nickel-Rich and Lithium-Rich Layered Oxide Cathodes: Progress and Perspectives. *Adv. Energy Mater.* **6**, n/a-n/a (2016).

5 Lee, J. *et al.* Unlocking the Potential of Cation-Disordered Oxides for Rechargeable Lithium Batteries. *Science (Washington, DC, U. S.)* **343**, 519-522 (2014).

6 Lee, J. *et al.* Reversible Mn2+/Mn4+ double redox in lithium-excess cathode materials. *Nature* **556**, 185-190 (2018).

7 Yabuuchi, N. *et al.* Origin of stabilization and destabilization in solid-state redox reaction of oxide ions for lithium-ion batteries. *Nat. Commun.* **7**, 13814 (2016).

8 Clément, R. J., Lun, Z. & Ceder, G. Cation-disordered rocksalt transition metal oxides and oxyfluorides for high energy lithium-ion cathodes. *Energy Environ. Sci.* **13**, 345-373 (2020).

9 Yabuuchi, N. *et al.* High-capacity electrode materials for rechargeable lithium batteries: Li3NbO4-based system with cation-disordered rocksalt structure. *Proc. Natl. Acad. Sci.* **112**, 7650-7655 (2015).

10 Kan, W. H. *et al.* Understanding the Effect of Local Short-Range Ordering on Lithium Diffusion in Li1.3Nb0.3Mn0.4O2 Single-Crystal Cathode. *Chem* **4**, 2108-2123 (2018).

11 Chen, D., Kan, W. H. & Chen, G. Understanding Performance Degradation in Cation-Disordered Rock-Salt Oxide Cathodes. *Adv. Energy Mater.* **9**, 1901255 (2019).

12 Seo, D.-H. *et al.* The structural and chemical origin of the oxygen redox activity in layered and cation-disordered Li-excess cathode materials. *Nat Chem* **8**, 692-697 (2016).

13 Lee, J. *et al.* A new class of high capacity cation-disordered oxides for rechargeable lithium batteries: Li-Ni-Ti-Mo oxides. *Energy Environ. Sci.* **8**, 3255-3265 (2015).

14 Kan, W. H. *et al.* Unravelling Solid-State Redox Chemistry in Li1.3Nb0.3Mn0.4O2 Single-Crystal Cathode Material. *Chem. Mater.* **30**, 1655-1666 (2018).

15 Assat, G. & Tarascon, J.-M. Fundamental understanding and practical challenges of anionic redox activity in Li-ion batteries. *Nature Energy* **3**, 373-386 (2018).

16 Gent, W. E. *et al.* Coupling between oxygen redox and cation migration explains unusual electrochemistry in lithium-rich layered oxides. *Nat. Commun.* **8**, 2091 (2017).

17 Zhou, K. *et al.* Elucidating and Mitigating the Degradation of Cationic–Anionic Redox Processes in Li1.2Mn0.4Ti0.4O2 Cation-Disordered Cathode Materials. *ACS Appl. Mater. Interfaces* **11**, 45674-45682 (2019).

18 Cambaz, M. A. *et al.* Understanding the Origin of Higher Capacity for Ni-Based Disordered Rock-Salt Cathodes. *Chem. Mater.* **32**, 3447-3461 (2020).

19 Kobayashi, Y. *et al.* Activation and stabilization mechanisms of anionic redox for Li storage applications: Joint experimental and theoretical study on Li2TiO3–LiMnO2 binary system. *Mater Today* **37**, 43-55 (2020).

20 Luo, M. *et al.* Identifying the anionic redox activity in cation-disordered Li1.25Nb0.25Fe0.50O2/C oxide cathodes for Li-ion batteries. *J. Mater. Chem. A* **8**, 5115-5127 (2020).

21 Yamamoto, K. *et al.* Charge Compensation Mechanism of Lithium-Excess Metal Oxides with Different Covalent and Ionic Characters Revealed by Operando Soft and Hard X-ray Absorption Spectroscopy. *Chem. Mater.* **32**, 139-147 (2020).

22 Lee, J. *et al.* Mitigating oxygen loss to improve the cycling performance of high capacity cation-disordered cathode materials. *Nat. Commun.* **8**, 981 (2017).

23 Kitchaev, D. A. *et al.* Design principles for high transition metal capacity in disordered rocksalt Li-ion cathodes. *Energy Environ. Sci.* **11**, 2159-2171 (2018).

24 Lun, Z. *et al.* Improved Cycling Performance of Li-Excess Cation-Disordered Cathode Materials upon Fluorine Substitution. *Adv. Energy Mater.* **9**, 1802959 (2019).

25 Lun, Z. *et al.* Design Principles for High-Capacity Mn-Based Cation-Disordered Rocksalt Cathodes. *Chem* **6**, 153-168 (2020).

26 House, R. A. *et al.* Lithium manganese oxyfluoride as a new cathode material exhibiting oxygen redox. *Energy Environ. Sci.* **11**, 926-932 (2018).

27 Ouyang, B. *et al.* Effect of Fluorination on Lithium Transport and Short-Range Order in Disordered-Rocksalt-Type Lithium-Ion Battery Cathodes. *Adv. Energy Mater.* **10**, 1903240 (2020).

28 Ahn, J., Chen, D. C. & Chen, G. Y. A Fluorination Method for Improving Cation-Disordered Rocksalt Cathode Performance. *Adv. Energy Mater.* **10**, 2001671 (2020).

29 Urban, A., Abdellahi, A., Dacek, S., Artrith, N. & Ceder, G. Electronic-Structure Origin of Cation Disorder in Transition-Metal Oxides. *Phys. Rev. Lett.* **119**, 176402 (2017).

30 Chen, D. *et al.* Role of Redox-Inactive Transition-Metals in the Behavior of Cation-Disordered Rocksalt Cathodes. *Small* **16**, 2000656 (2020).

31 Tu, X. Y. & Shu, K. Y. X-ray diffraction study on phase transition of orthorhombic LiMnO2 in electrochemical conversions. *J. Solid State Electrochem.* **12**, 245-249 (2008).

32 Ye, Y. *et al.* X-ray spectroscopies studies of the 3d transition metal oxides and applications of photocatalysis. *MRS Communications* **7**, 53-66 (2017).

33 Henderson, G. S., Liu, X. & Fleet, M. E. A Ti L-edge X-ray absorption study of Ti-silicate glasses. *Phys. Chem. Miner.* **29**, 32-42 (2002).

34 Qiao, R., Chin, T., Harris, S. J., Yan, S. & Yang, W. Spectroscopic fingerprints of valence and spin states in manganese oxides and fluorides. *Current Applied Physics* **13**, 544-548 (2013).

35 Ikeno, H. *et al.* Theoretical Fingerprints of Transition Metal L2,3 XANES and ELNES for Lithium Transition Metal Oxides by ab Initio Multiplet Calculations. *J. Phys. Chem. C* **115**, 11871-11879 (2011).

36 Kim, J.-M. & Chung, H.-T. The first cycle characteristics of Li[Ni1/3Co1/3Mn1/3]O2 charged up to 4.7 V. *Electrochim. Acta* **49**, 937-944 (2004).

37 Kataoka, R., Kojima, T. & Takeichi, N. Electrochemical Property of Li-Mn Cation Disordered Li-Rich Li2MnO3 with NaCl Type Structure. *J. Electrochem. Soc.* **165**, A291-A296 (2018).

38 Qiao, R. *et al.* Distinct Solid-Electrolyte-Interphases on Sn (100) and (001) Electrodes Studied by Soft X-Ray Spectroscopy. *Advanced Materials Interfaces* **1**, 1300115 (2014).

39 Liu, W. *et al.* Countering Voltage Decay and Capacity Fading of Lithium-Rich Cathode Material at 60 °C by Hybrid Surface Protection Layers. *Adv. Energy Mater.* **5**, 1500274-n/a (2015).

40 Boulineau, A., Simonin, L., Colin, J.-F., Bourbon, C. & Patoux, S. First Evidence of Manganese–Nickel Segregation and Densification upon Cycling in Li-Rich Layered Oxides for Lithium Batteries. *Nano Lett.* **13**, 3857-3863 (2013).

41 Jung, S.-K. *et al.* Understanding the Degradation Mechanisms of LiNi0.5Co0.2Mn0.3O2 Cathode Material in Lithium Ion Batteries. *Adv. Energy Mater.* **4**, 1300787 (2013).

42 Toby, B. H. & Von Dreele, R. B. GSAS-II: the genesis of a modern open-source all purpose crystallography software package. *J. Appl. Crystallogr.* **46**, 544-549 (2013).

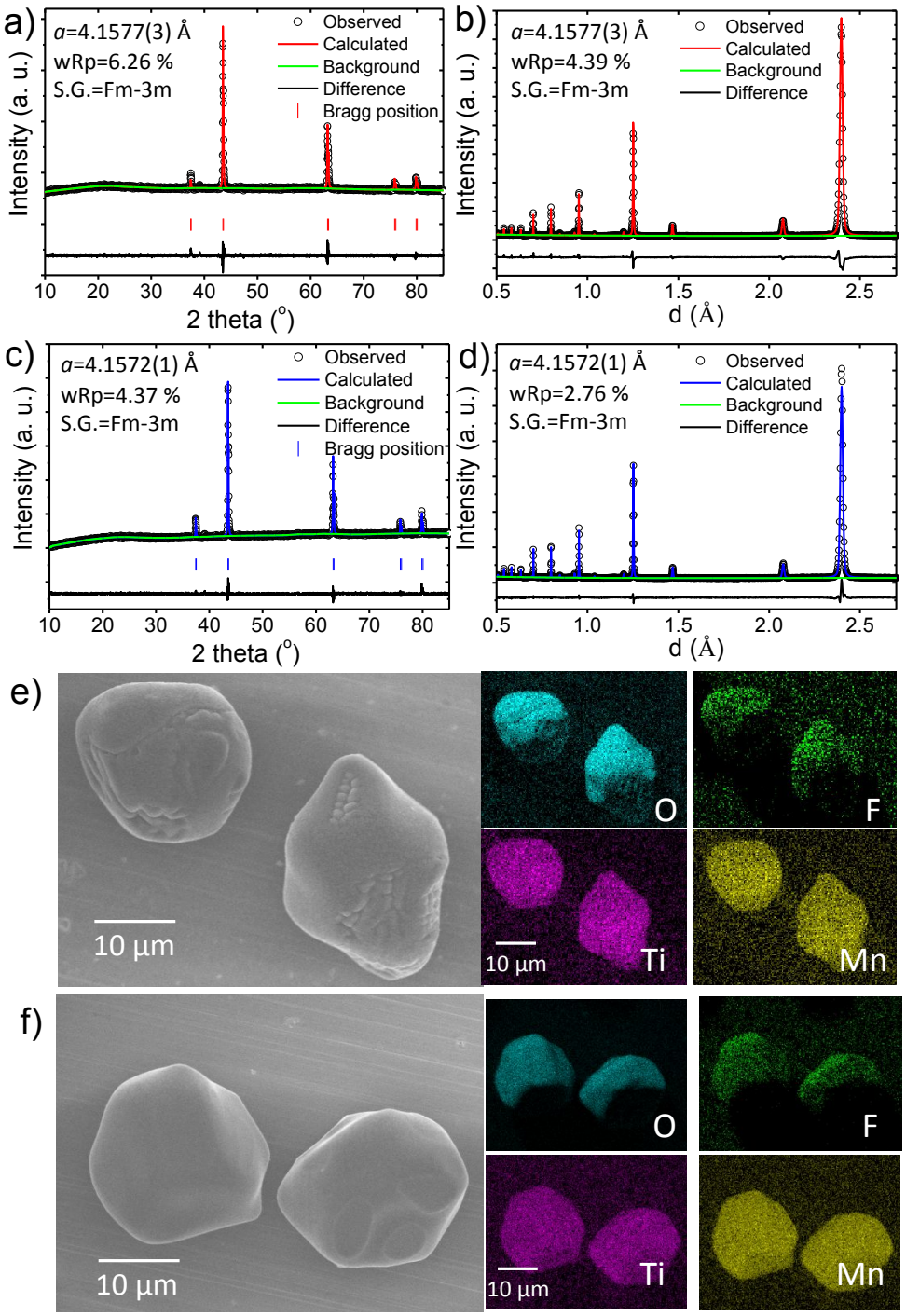

Figure 1. Refinement of (a, c) X-ray and (b, d) neutron diffraction patterns collected on pristine LTMOF3.25 (a, b) and LTMOF2.0 (c, d), e) and f) SEM images and EDX elemental mapping for pristine LTMOF3.25 and LTMOF2.0, respectively.

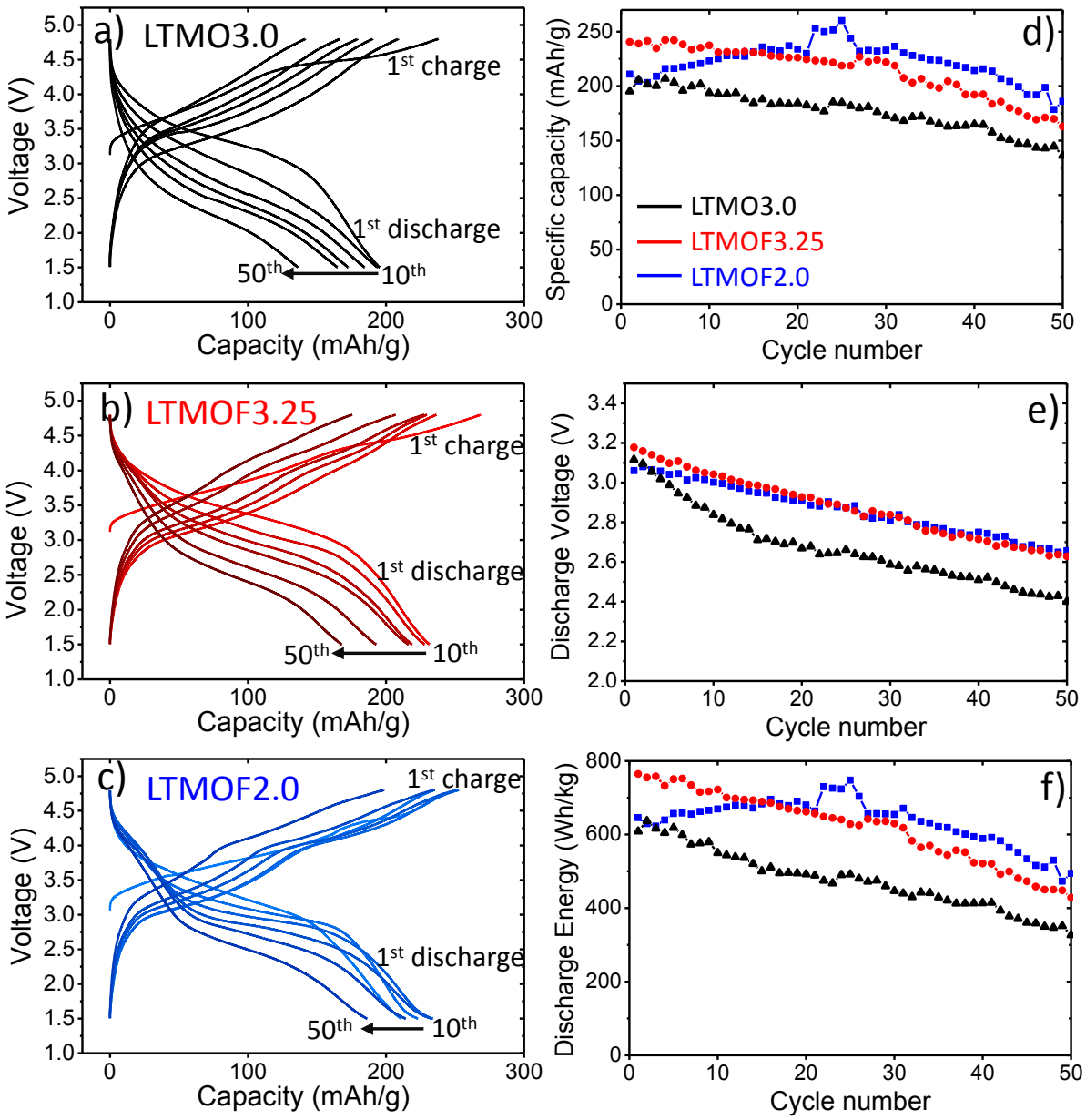

Figure 2. Voltage profiles of: a) LTMO3.0, b) LTMOF3.25 and c) LTMOF2.0 half cells during the first 50 cycles. Data plotted for the 1st cycle and every 10th cycle afterwards. d-f) comparison of cathode discharge capacity, average discharge voltage and discharge energy. The current density was 10 mA/g.

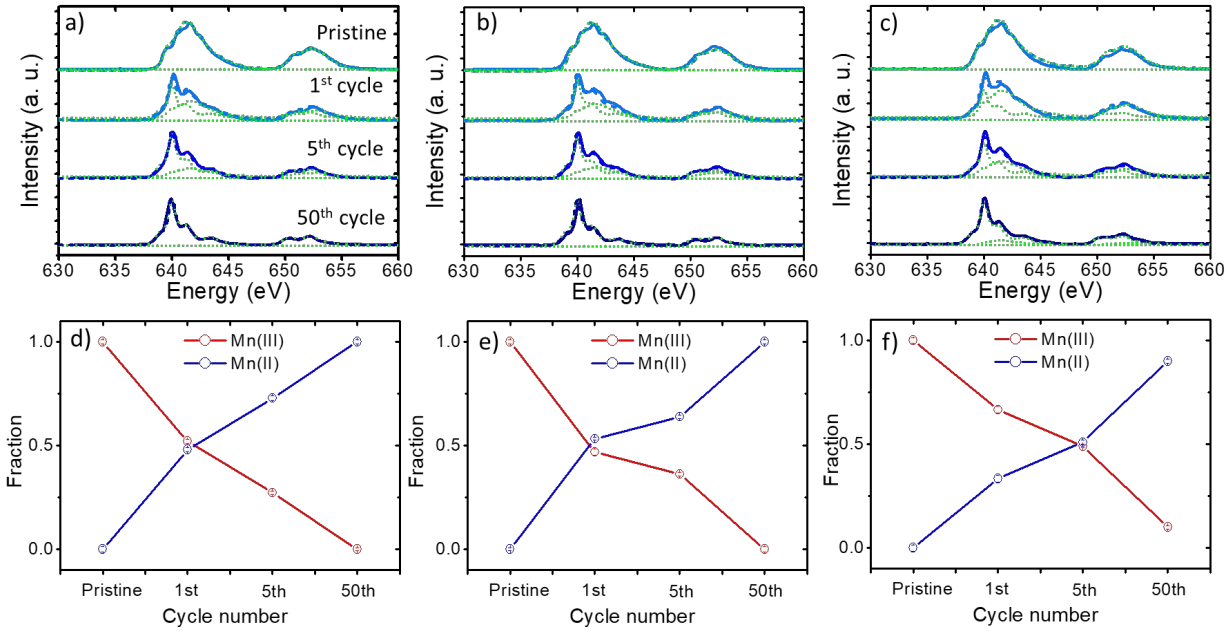

Figure 3. Mn *L*-edge XAS profiles collected at the discharged state after various cycles: a) LTMO3.0, b) LTMOF3.25 and c) LTMOF2.0, d-f) comparison of Mn(II) and Mn(III) fraction in LTMO3.0, LTMOF3.25 and LTMOF2.0, respectively. Spectra were collected in the TEY mode.

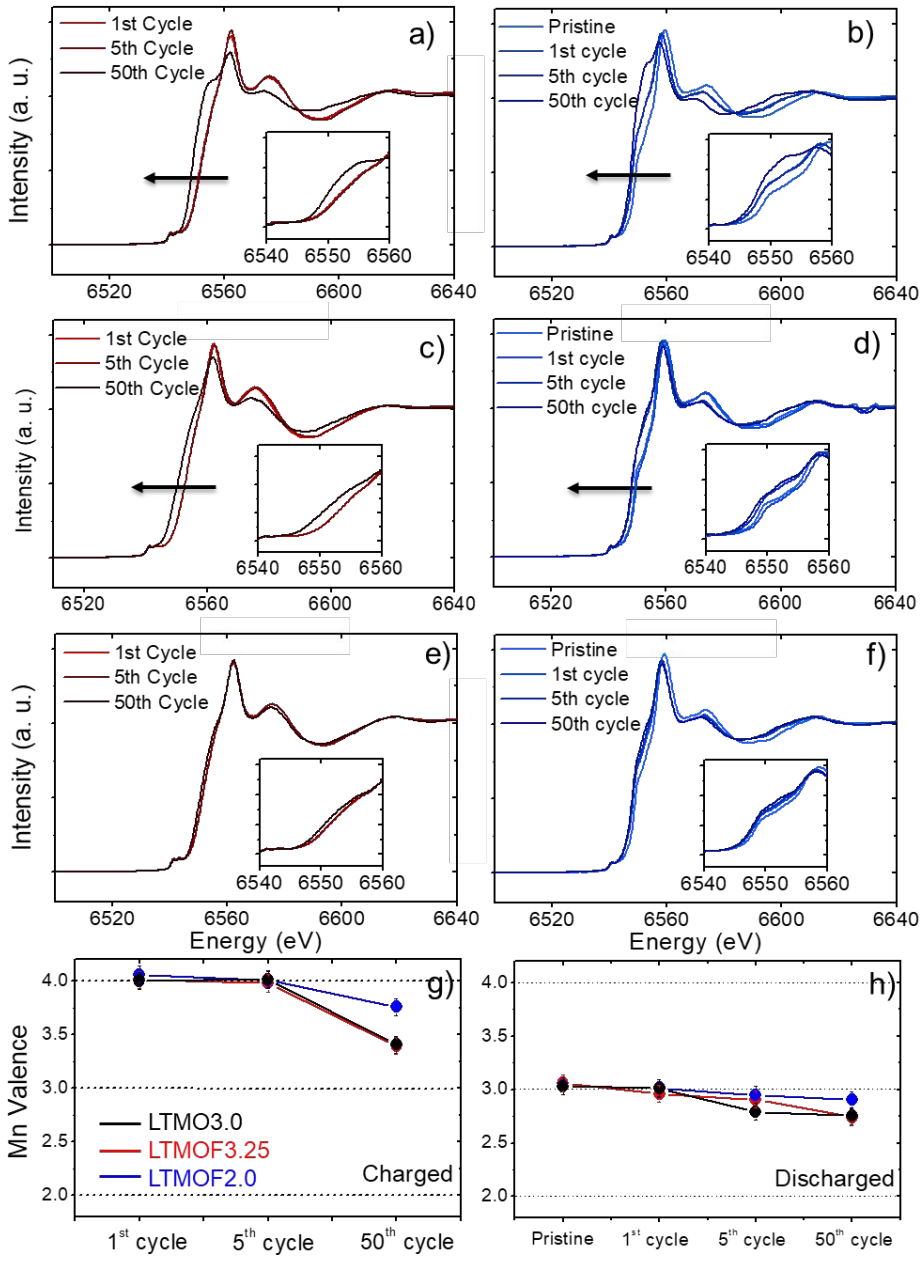

Figure 4. Mn *K*-edge XANES profiles collected on (a, b) LTMO3.0, (c, d) LTMOF3.25 and (e, f) LTMOF2.0 cathodes at the charged state (a, c, e) and discharged state (b, d, f) after 1, 5 and 50 cycles. Insets show the expanded view on edge profiles. g-h) average Mn oxidation state at the charged and discharged states, respectively.

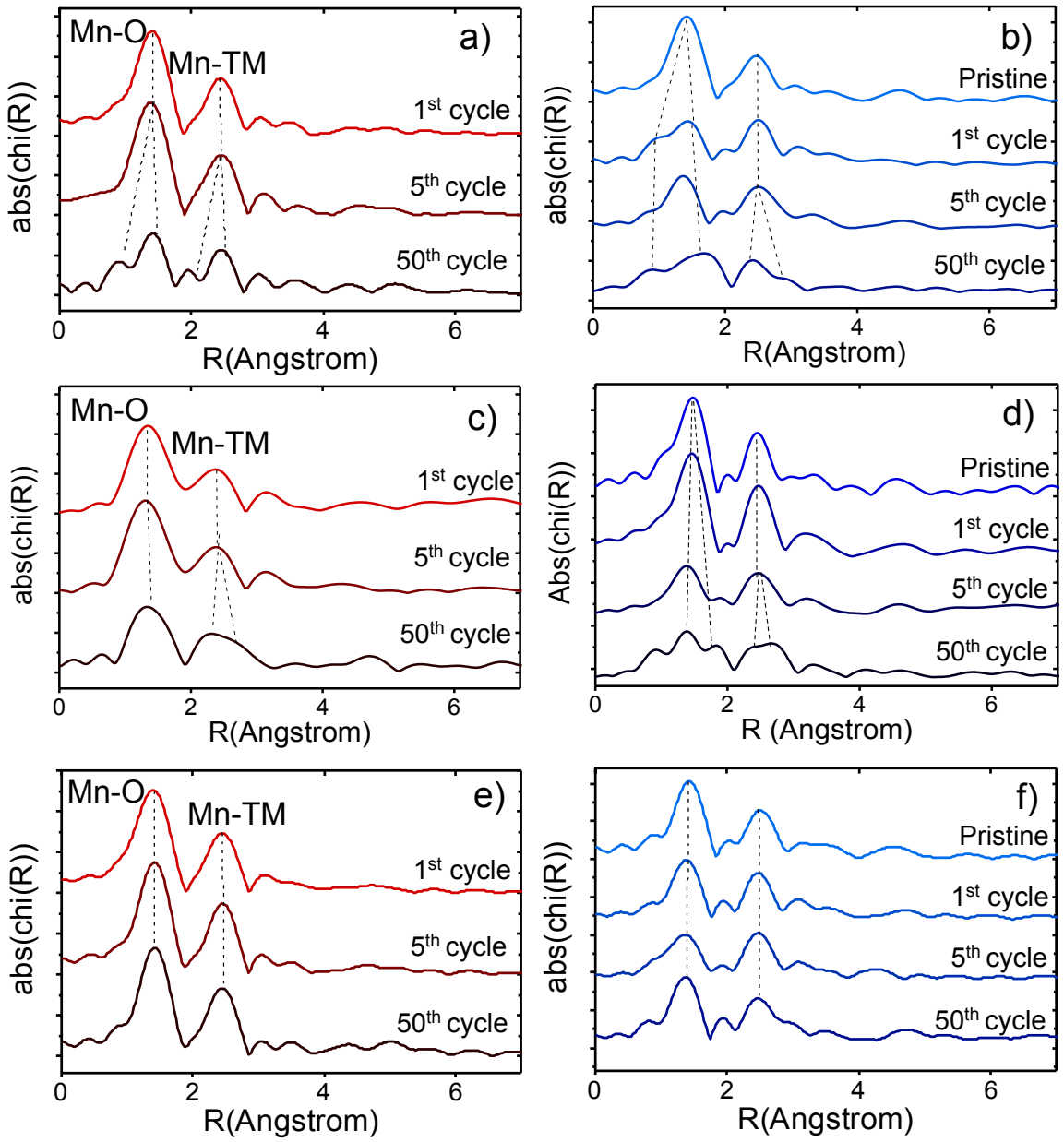

Figure 5. Mn *K*-edge EXAFS profiles collected on (a, b) LTMO3.0, (c, d) LTMOF3.25 and (e, f) LTMOF2.0 cathodes at the charged state (a, c, e) and discharged state (b, d, f) after 1, 5 and 50 cycles.

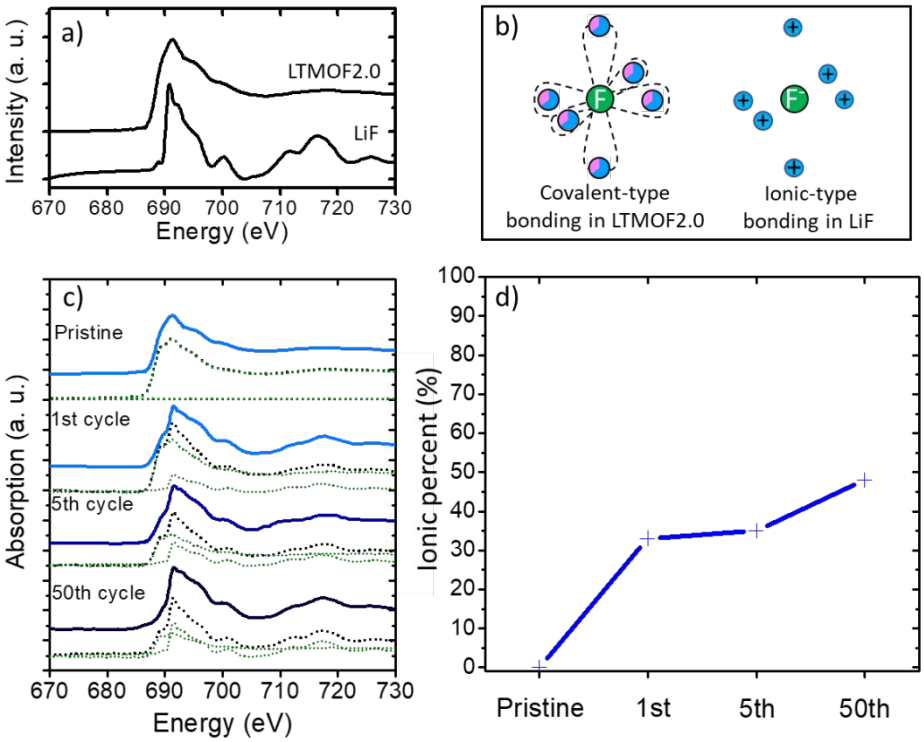

Figure 6. a) Comparison of F *K*-edge XAS data collected on pristine LTMOF2.0 and LiF standard, b) A schematic shows the covalent-type and ionic-type bonding environment of F, c) F *K*-edge XAS data collected on discharged LTMOF2.0 cathodes after various cycles, and d) evolution of ionic fluorine fraction as a function of cycle number. All spectra were collected in the TEY mode. All spectra in c) were fitted *via* linear combination fitting of covalent and ionic components (green lines) and the fitted spectra are shown in dotted lines.

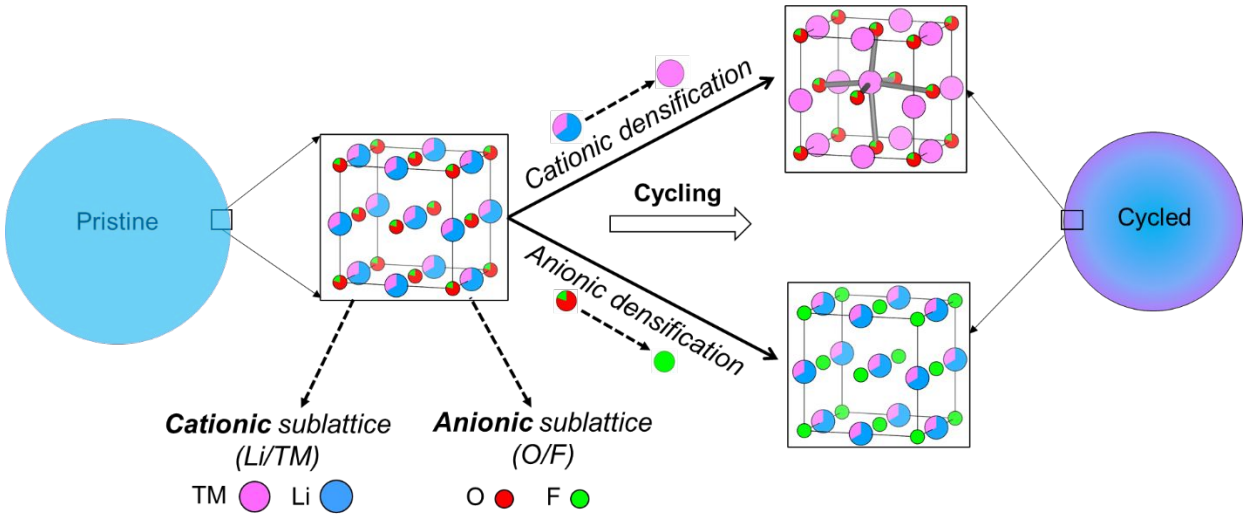

Figure 7. A schematic showing concerted cationic and anionic densification process in F-DRX. Blue, pink, red and green circles represent Li, TM, O and F respectively.

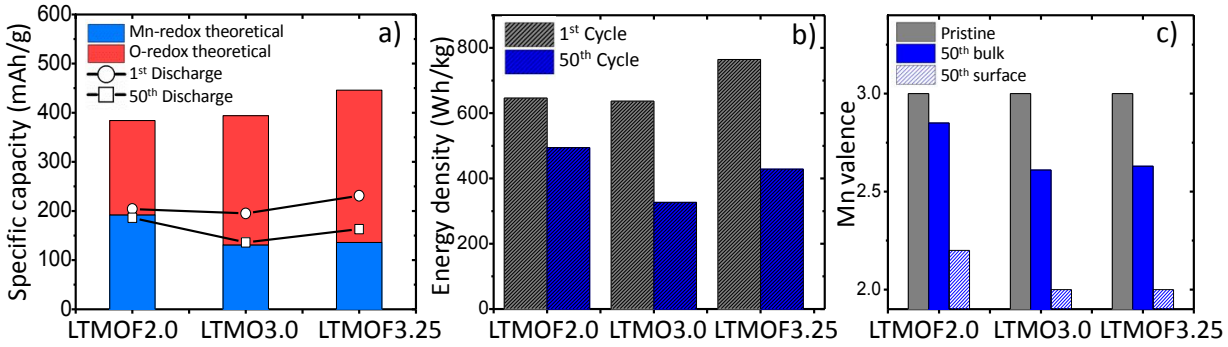

Figure 8. a) Comparison of theoretical and experimental capacities obtained on the DRX cathodes, b) comparison of discharge energy after 1st and 50th cycle, and c) comparison of Mn valence at the indicated states.